Environmental Science & Technology

pubs.acs.org/est

Article

Underappreciated Soil NO_x Emissions Amplify Background O_3 Pollution During Compound Dry-Hot Extremes in North China

Zhao Yang,[▽] Tong Sha,[*,▽] Feng Wu, Qingcai Chen, K. Folkert Boersma, Jun Wang, and Yan-Lin Zhang

Cite This: *Environ. Sci. Technol.* 2026, 60, 20484−20495

Read Online

ACCESS | Metrics & More | Article Recommendations | Supporting Information

ABSTRACT: Increasingly frequent compound dry-hot extremes (CDHEs) are influencing atmospheric chemistry through land-atmosphere feedback. Here we show that summertime surface ozone (O_3) concentrations across natural background regions of North China (>35°N) unexpectedly exceed those in urban areas, accompanied by an increasing trend in tropospheric NO_2 vertical column densities (VCDs). This compelling spatial anomaly confirms that natural nitrogen oxides (NO_x) sources, particularly soil NO_x emissions (SNO_x), may play a pivotal role in driving O_3 formation. To test this hypothesis, numerical experiments with the Unified Inputs for WRF-Chem (UI-WRF-Chem) are conducted, in which the SNO_x scheme as a function of the soil temperature and moisture is developed with the constraint of satellite-retrieved SNO_x fluxes in 2018−2024. During a severe CDHE in summer 2022, extreme dry-hot forcings triggered potent SNO_x in natural backgrounds. Although natural soils have substantially lower nitrogen availability than croplands, their SNO_x could contribute to 43% of O_3 production. Our study highlights the urgent need to incorporate NO_x emissions from natural lands in air quality management strategies as CDHEs are projected to intensify under climate change.

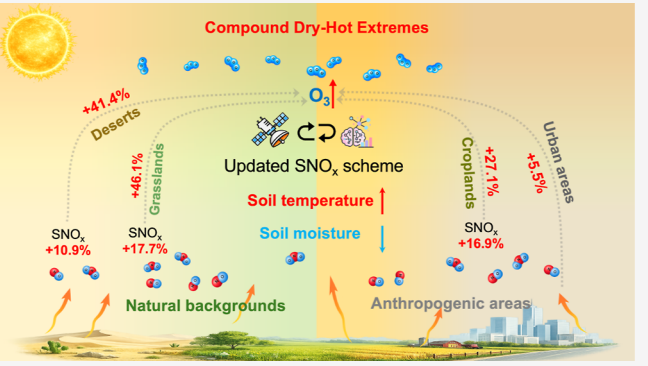

KEYWORDS: *natural sources, soil nitrogen emissions, model simulations, ozone pollution, extreme climate change*

1. INTRODUCTION

As a major natural contributor to the global NO_x (NO + NO_2) budget, soil NO_x emissions (SNO_x) serve as a critical biogeochemical process linking the terrestrial nitrogen cycle with atmospheric chemistry, playing a pivotal role in modulating photochemical reactions and ozone (O_3) formation.[1−4] The magnitude and variability of these emissions are jointly controlled by microbial nitrification and denitrification, substrate availability, environmental and meteorological conditions, specifically soil temperature, soil moisture, and precipitation-induced emission pulse from dry soils.[5] Driven by climate change, increasingly frequent extreme events, particularly compound dry-hot extremes (CDHEs), are profoundly altering land-atmosphere exchange processes,[6,7] which may modulate the NO_x emissions from soils and thereby influence tropospheric atmospheric chemistry.[8,9] However, existing studies have largely focused on the impacts of agricultural fertilization and anthropogenic nitrogen inputs on SNO_x, quantitative assessments of how climate-driven meteorological extremes modulate SNO_x and subsequently influence O_3 pollution remain limited.[3,10,11]

In recent years, CDHEs have shown an increasing trend in frequency, intensity, and spatial extent across China.[12] Notably, the high-risk zones of CDHEs are shifting northward,[12] rendering North China more susceptible to persistent hot and dry regimes.[13−15] Under high temperatures and intense solar radiation, the vast natural landscapes in North China, especially deserts and grasslands, experience enhanced emissions of reactive nitrogen from soils, thereby accelerating the atmospheric nitrogen cycling.[16−19] These areas are also characterized by radiation-intensive photochemistry that facilitates rapid NO_x oxidation.[20] Accordingly, CDHE-amplified SNO_x undergo rapid chemical conversion, further aggravating local and downwind O_3 formation. A recent study demonstrated that the synergy of natural emissions, including soil reactive nitrogen (NO and HONO) and biogenic volatile organic compounds (BVOCs), significantly exacerbates O_3 pollution during CDHEs in eastern China, a region heavily dominated by mixed anthropogenic emissions and intensive agricultural activities, highlighting the importance of natural sources in regional photochemistry.[21] To our knowledge, studies about quantifying the impacts of CDHE-driven SNO_x change on O_3 pollution across natural regions are still limited.

Received: April 28, 2026
Revised: July 8, 2026
Accepted: July 8, 2026
Published: July 13, 2026

https://doi.org/10.1021/acs.est.6c06361
Environ. Sci. Technol. 2026, 60, 20484−20495

Moreover, widely adopted SNO_x parametrization schemes in current atmospheric chemical transport models, such as the Berkeley−Dalhousie Soil NO_x Parameterization (BDSNP)[22] and the Yienger and Levy (1995) empirical scheme (YL95),[23] cannot adequately characterize emission responses under hot and dry conditions. Specifically, the response of SNO_x to high temperatures is generally represented using a fixed threshold, which fails to capture the continuous variation in SNO_x at elevated temperatures.[24] Additionally, the soil moisture response is commonly parametrized using a uniform soil moisture optimum and inhibition strength regardless of soil types. However, field evidence demonstrates that the optimal soil moisture for SNO_x varies spatially, ranging from 15% to 65%.[25] For natural background regions where summertime 2 m air temperatures (T2) frequently exceed 30 °C and land cover types are highly heterogeneous, these simplified representations of the responses to high-temperature and soil-moisture may introduce substantial biases in SNO_x estimates within critical soil temperature-moisture regimes. These limitations thus constrain the accurate estimation of SNO_x variability and its impacts on O_3 pollution during severe CDHEs.[26−28]

In this study, we derive top-down SNO_x inventory over North China during the summer of 2018−2024, constrained by TROPOMI-observed NO_2 vertical column densities (VCDs) (the study region is shown in Figure 2b). Within the Berkley-Dalhousie Iowa Soil NO Parameterization (BDISNP) framework, we apply Interpretable Machine Learning (ML) algorithms to rigorously optimize biome-specific soil temperature-moisture response functions for dominant natural land cover types (deserts, grasslands, and croplands), aiming to improve the representation of SNO_x variability under dry-hot conditions. We then select June 2022, a month characterized by intense and frequent CDHEs in North China, and apply this updated SNO_x scheme to quantify the impacts of CDHE-driven SNO_x on O_3 pollution. Our study elucidates the complex variability of SNO_x in natural regions and highlights its critical role in amplifying O_3 pollution under extreme climate events.

2. MATERIALS AND METHODS

2.1. Data Sources and Preprocessing

Tropospheric NO_2 VCDs are obtained from the Sentinel-5 Precursor TROPOspheric Monitoring Instrument (Sentinel-5P/TROPOMI) Level 2 NO_2 product, with the satellite overpass time around 13:30 local time (LT). We utilize the Reprocessed (RPRO) v2.4.0 data set until 25 July 2022 and the Offline (OFFL) products thereafter (v2.4.0, v2.5.0, v2.6.0). The nadir spatial resolution is approximately 3.5 km × 7 km before 6 August 2019 and 3.5 km × 5.5 km afterward. According to the official product documentation, OFFL products in v2.5.0 differ from v2.4.0 only by a bug fix for snow/ice pixels; v2.6.0 may yield lower tropospheric NO_2 VCDs, especially in midlatitude winter. Since our study focuses on summer, the associated uncertainty may be smaller than in wintertime applications; nonetheless, the inclusion of products in v2.6.0 is still considered a potential source of uncertainty in the top-down inversion.[29] The raw orbital data are subjected to standardized quality control before analysis, and only pixels satisfying the following criteria are retained: quality flag value > 0.5,[30] cloud fraction ≤0.3, solar zenith angle ≤70°, and viewing zenith angle ≤70°.[31−34] Meteorological fields are derived from two ECMWF reanalysis products. Boundary layer height (BLH), surface pressure (SP), surface geopotential (Z), and pressure-level horizontal winds are obtained from ECMWF Reanalysis v5 (ERA5) at 0.25° × 0.25° resolution.[35] Hourly 2 m air temperature (T2) and total precipitation (TP) are obtained from the ERA5-Land reanalysis at 0.1° × 0.1° resolution.[36] The above data sets are utilized to retrieve SNO_x flux.

Land cover types are derived from the annual MODIS MCD12C1 product at 0.05° × 0.05° resolution, which categorizes 17 distinct land cover types.[37,38] Soil temperature and soil moisture are obtained from the Soil Moisture Active Passive (SMAP) Level 4 soil data set (9 km × 9 km, 3 hly). Fire activities are from the daily NASA FIRMS Visible Infrared Imaging Radiometer Suite (VIIRS) 375 m active fire product. Anthropogenic emissions are obtained from the Multiresolution Emission Inventory for China (MEIC) for the corresponding years (0.25° × 0.25°, monthly). Interannual nitrogen inputs are mapped by synthesizing provincial-level agricultural fertilizer statistics from the China Statistical Yearbook and annual total nitrogen deposition from Gao et al. (2023) at 0.25° × 0.25° resolution.[39] The above data sets are used to optimize the soil temperature-moisture response functions in the SNO_x scheme.

Ground-based observations, including daily maximum 8 h average (MDA8) O_3 and surface NO_2 concentrations, are obtained from the China National Environmental Monitoring Centre (CNEMC). Hourly 2 m air temperature is obtained from the China Meteorological Data Service Center. These measurements are used to evaluate model simulation performance. To mitigate the spatial sparsity of ground-based stations, we further incorporate the high-resolution MDA8 O_3 data set from the China High Air Pollutants (CHAP) product developed by Wei et al.[40]

To ensure spatiotemporal consistency among multisource data sets and model simulations, all variables are resampled to a 0.1° × 0.1 ° regular grid and synchronized with the overpass times of the TROPOMI satellite. Specifically, continuous scalar variables are resampled using bilinear interpolation, whereas vector variables such as wind fields are resampled using a momentum-conserving approach. Land cover types are matched using the nearest-neighbor method, with each 0.1° grid cell classified according to its dominant land cover type to facilitate subsequent land-cover-specific analysis. Active fire data are aggregated to the corresponding grid cells based on the total daily fire counts. Anthropogenic emissions are resampled using an area-conserving method to preserve regional total emissions.

2.2. Model Configurations

The Unified Inputs for WRF-Chem (UI-WRF-Chem) model, developed from the standard WRF-Chem v3.9.1,[41] is utilized in this study. The detailed information regarding the specific improvements integrated into the UI-WRF-Chem can be found in our previous study.[42] Meteorological and chemical initial and boundary conditions are provided by Modern-Era Retrospective analysis for Research and Applications, Version 2 (MERRA-2) with a spatial resolution of 0.625° × 0.5°,[43] and soil moisture and temperature are initialized from Global Land Data Assimilation System (GLDAS) at a 0.25° × 0.25° resolution.[44] For emission inventories, anthropogenic emissions are from MEIC for the year 2022, biomass burning emissions are from FINN v1.5,[45] and biogenic emissions are calculated online using MEGAN v2.1.[46] The selected physical parametrizations include the Morrison two-moment microphysics scheme,[47] the Grell 3-D cumulus scheme,[48] the RRTMG longwave and shortwave radiation schemes,[49] the Yonsei University planetary boundary layer scheme,[50] and the Noah land surface model.[51] The Regional Acid Deposition Model, Version 2 (RADM2) for gas-phase chemistry,[52] coupled with the Modal Aerosol Dynamics Model for Europe (MADE) and the Secondary Organic Aerosol Model (SORGAM) aerosol modules with aqueous reactions, is chosen.[41,53,54] We conducted one domain simulation over North China and its surrounding regions (66.2−138.4°E, 30.9−55.6°N) at a horizontal resolution of 12 km, with 399 × 192 grid cells. There are 48 vertical levels from the surface to 50 hPa, and 4 soil layers. Simulations are conducted for two periods (30 May to 31 August 2021, and 30 May to 30 June 2022) using a monthly simulation approach, with the first 2 days of each simulation period as spin-up. The study domain is focused on the region of China north of 35°N.

To evaluate the revised soil temperature-moisture response function within the BDISNP scheme and quantify the contribution of SNO_x to O_3 formation across natural regions during CDHEs, three experiments are conducted, i.e., Default, Updated, and $NoSNO_x$

https://doi.org/10.1021/acs.est.6c06361
Environ. Sci. Technol. 2026, 60, 20484−20495

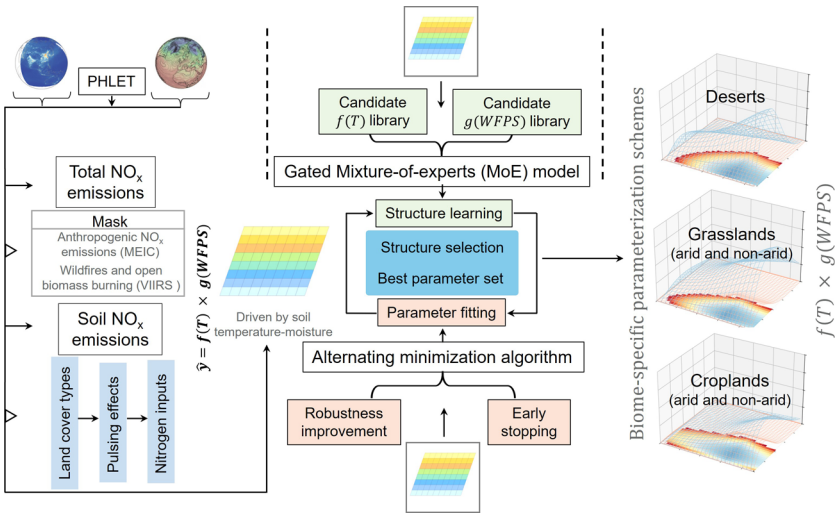

Figure 1. Overview of the satellite-constrained daily SNO_x inversion and the subsequent parametrization framework with structure learning and land-cover-specific fitting.

(Table S1). Default is the baseline simulation using the original BDISNP scheme implemented in the UI-WRF-Chem model.[2] Update is the simulation applying the newly developed soil temperature-moisture response functions to accurately represent SNO_x variations under extreme dry-hot conditions. $NoSNO_x$ is identical to the Updated except that SNO_x are excluded.

2.3. SNO_x Inversion and Soil Temperature-Moisture Responses Functions Improvement

Following the PHLET (Peking University High-Resolution Lifetime-Emission-Transport) algorithm,[55] we derived daily top-down total NO_x emissions at 0.1° resolution for summers (June-August) during 2018−2024, using TROPOMI-observed tropospheric NO_2 VCDs and ERA5 meteorological fields. The detailed inversion of total NO_x emissions is described in Text S1. To robustly isolate NO_x emissions from soils, we implement a rigorous masking and correction method. Grid cells strongly influenced by anthropogenic sources are excluded, which are defined as monthly total anthropogenic NO_x emissions exceeding 0.5 tons based on the MEIC inventory. To eliminate the impacts of wildfires and open biomass burning, fire-affected grid cells are identified and strictly masked out utilizing the VIIRS active fire product. The above procedures ultimately yield a sample of NO_x emissions mainly attributable to soils.

The BDISNP scheme is parametrized as a baseline emission term and a set of environmental and meteorological response factors, which include the soil temperature and moisture, precipitation-induced emission pulse from dry soils, and canopy effects.[26,56] We follow the same general framework, retaining the baseline emission term and the original treatments of the pulsing factor and canopy reduction effects, while only update soil temperature and moisture SNO_x response factors using satellite-constrained top-down SNO_x samples over North China during 2018−2024. To isolate the SNO_x response factors driven specifically by soil temperature and moisture, the samples are further screened from three aspects. (1) Treatment of different land cover types: analyses are performed separately by dominant land cover types (e.g., deserts, grasslands, and croplands) to minimize cross-biome discrepancies arising from varying baseline emission coefficients, available nitrogen in soils, and canopy reduction effects.[27] (2) Removal of pulsing effects: SNO_x samples influenced by precipitation- or irrigation-induced pulses are excluded. Given that soil pulses typically persist for 1−2 days,[56−58] we combine ERA5 precipitation and SMAP surface soil moisture to identify potential pulse events. Specifically, an accumulated precipitation exceeding 3.0 mm within the 12 h preceding the TROPOMI overpass time is defined as a precipitation-induced pulsing event. Similarly, a daily increment in surface soil moisture ($\Delta\theta$) larger than 0.03 $m^3\ m^{-3}$ is defined as an irrigation-induced rewetting pulse. SNO_x samples on the day of pulse occurrence and the subsequent 2 days are excluded.[59] (3) Calibration of interannual nitrogen inputs for soils: to eliminate the interference from interannual variations in fertilizer and nitrogen deposition on soil nitrogen availability, we construct an interannual calibration factor (M_{year}) using the year 2022 as the baseline year. M_{year} accounts for the spatiotemporal variations in biome-specific baseline emissions (A_{biom}), nitrogen fertilizer application ($Fert_N$), and dry and wet nitrogen deposition (depN) across different land cover types (Text S2 and Figures S2 and S3 for details).

Based on prior knowledge of the biogeochemical mechanisms underlying SNO_x, we construct a candidate library of soil temperature-moisture response functions. Soil moisture herein is quantified as water-filled pore space (WFPS), defined as volumetric soil moisture (VSM) divided by soil porosity (Table S2) and ranges from 0 to 1.[27,56] Specifically, the candidate soil temperature response functions ($f(T)$) are designed to characterize the temperature-driven enhancement of SNO_x and its saturation under high-temperature conditions, whereas the candidate soil moisture response functions (g(WFPS)) are designed to represent a unimodal response, characterized by enhanced emissions under moderately dry conditions and suppressed emissions under excessive wetness.[25,28,60] To identify the optimal functional architectures from this library, we apply a physics-informed ML approach utilizing a gated mixture-of-experts (MoE) model. Using soil temperature (T) and WFPS as inputs, the MoE model is trained against the filtered SNO_x response samples driven exclusively by soil temperature-moisture ($\hat{y}$). These samples are categorized by land cover types and randomly divided into a parameter optimization subset (80%) and a structure selection subset (20%). The former is used for initial tuning of continuous parameters, while the latter is used to update the MoE gating weights that indicate the relative support for individual candidate structures. The structures with the highest final gating weights are selected as the optimal forms of $f(T)$ and g(WFPS), which are subsequently applied to biome-specific parameter optimization through an alternating minimization algorithm.[61−63] To accurately characterize spatial heterogeneity, these models are trained independently for deserts (36.8% of the study domain), grasslands (32.6%), and croplands (17.5%), collectively accounting for approximately 87% of North China (Text S3 for details). Ultimately, this ML algorithm converged on a soft-saturation-Rayleigh functional structure, which aligns with the complex and dynamic biogeochemical controls of SNO_x.[56,64,65] The soft-saturation soil temperature term robustly characterizes the initial emission enhancement and gradual limitation under extreme-event conditions. The Rayleigh-type soil moisture term captures the unimodal response to WFPS, including emission suppression under excessive dryness or wetness.[26,66] The final functional form is expressed as follows

https://doi.org/10.1021/acs.est.6c06361
Environ. Sci. Technol. 2026, 60, 20484−20495

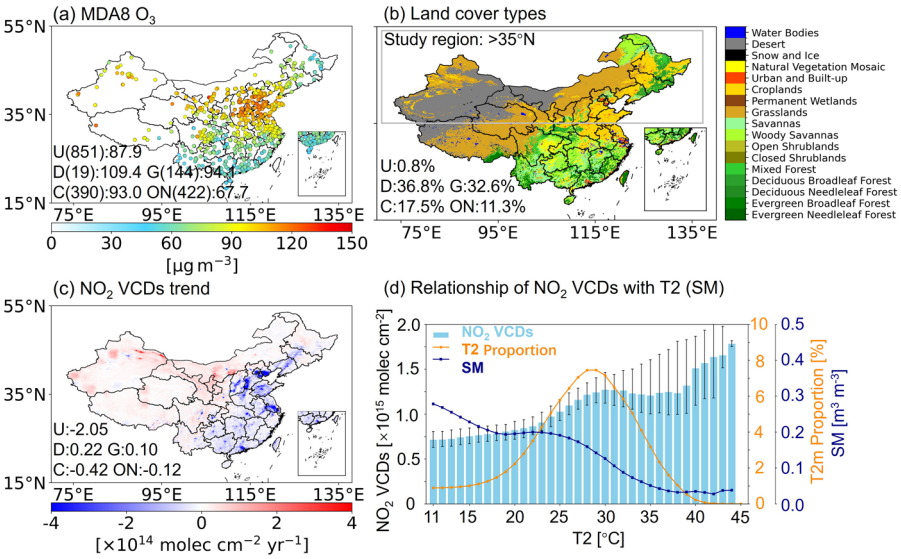

Figure 2. (a) Spatial distribution of mean summertime (June−August) MDA8 O_3 from CNEMC measurements in China during 2018−2024. (b) Spatial distribution of land cover types in China for the year 2022. The dashed box outlines the study region. (c) Variation trends in summertime tropospheric NO_2 VCDs from TROPOMI satellite observations in China during 2018−2024. (d) Relationship between NO_2 VCDs and T2 over North China during the same period. Bars represent the mean NO_2 VCDs within each T2 bin; the orange and blue curves denote the sample proportion and the corresponding mean soil moisture for each T2 bin, respectively. Statistics in panels (a) and (c) show the mean values across different land cover types, where "U", "D", "G", "C", and "ON" denote Urban, Deserts, Grasslands, Croplands, and Other natural land covers, respectively. Here, "other natural land covers" refers to land cover types other than "Urban", "Deserts", "Grasslands", "Croplands", "Water", and "Snow and Ice". The numbers in parentheses in panel (a) indicate the number of sites.

$$\hat{y} = A \times f(T) \times [g(\mathrm{WFPS})]^{\alpha}$$

where $\hat{y}$ is the model-predicted SNO_x response factors, A is an overall scaling coefficient, and α governs the amplitude of the soil moisture response (all variables are dimensionless).

$$f(T) = (1 - \omega) \times \exp(aT^*) + \omega \times \exp(aT_{\mathrm{sat}})$$

$$\omega = \frac{1}{1 + \exp\left(-\frac{T^* - T_{\mathrm{sat}}}{s}\right)}$$

$$T^* = \min(\max(T, 0), T_{\mathrm{cap}})$$

where a is the intensity of the soil temperature response (°C^{-1}); T_{sat} and s denote the soil temperature saturation threshold (°C) and the saturation transition rate (°C), respectively; T_{cap} denotes the maximum effective soil temperature (°C), fixed at 45 °C in this study.

$$g(\mathrm{WFPS}) = \mathrm{WFPS} \cdot e^{-k(\mathrm{WFPS})^2}$$

where k is a peak-decay characteristic of the soil moisture response.

The optimized parameters across the three dominant biomes are summarized in Table S3. Deserts exhibit the highest scaling coefficient. Grasslands and croplands are further divided into arid and nonarid subclasses, and the results show pronounced heterogeneity in soil moisture response characteristics within each land cover type. While the soil temperature-moisture response functions were robustly optimized using the full satellite-constrained SNO_x data set, we acknowledge that the limited number of extreme dry-hot samples may introduce uncertainties at the extreme boundaries of these functions. Figure 1 presents a schematic overview of our integrated framework, showing the satellite-constrained top-down inversion of SNO_x, the ML-based structure selection and parameter optimization of the soil temperature-moisture response functions, and the implementation of biome-specific parametrization schemes for deserts, grasslands, and croplands.

2.4. Definition of Compound Dry-Hot Events

Utilizing ERA5-land data for summer (June−August) during 2018−2024, we identify a CDHE when the following three criteria are simultaneously satisfied at the grid-cell level: (1) the daily maximum 2 m air temperature ($T2_{\mathrm{max}}$) exceeds both an absolute threshold of 30 °C and its local the 90th percentile; (2) soil moistures are below an absolute threshold of 0.15 m3 m^{-3} and its local 20th percentile; (3) these dry-hot conditions persist for at least 3 consecutive days.[67−70] The selection of these percentile thresholds for both $T2_{\mathrm{max}}$ and soil moisture is characterized by extreme heat and anomalous dryness relative to the summertime climatology of North China during this period.

3. RESULTS AND DISCUSSION

3.1. High Surface O_3 and Increasing NO_2 VCDs in Natural Background Regions

Figure 2a illustrates the spatial distribution of summertime surface MDA8 O_3 during 2018−2024 based on CNEMC measurements. Although urban regions exhibit relatively high O_3 pollution (87.9 μg m^{-3}), remote and sparsely monitored natural backgrounds display comparable or even higher O_3 concentrations. Specifically, the highest MDA8 O_3 levels are observed over deserts (109.4 μg m^{-3}), followed by grasslands (94.1 μg m^{-3}), croplands (93.0 μg m^{-3}), and other natural land cover types (67.7 μg m^{-3}). Given the sparse distribution of CNEMC sites in natural regions, we corroborate these ground-based observations using the high-resolution CHAP data set developed by Wei et al.[40] (Figure S3a). This fused data set also confirms that summertime O_3 concentrations over northern deserts and grasslands rival those of urban areas. One might hypothesize that downward transport of O_3-rich air from the free troposphere or stratosphere can episodically enhance surface O_3. However, such influences are highly event-dependent, more pronounced during winter−spring or spring-time intrusion events, and generally weaker in the boundary layer than in the free and upper troposphere.[71−74] Thus, this mechanism is unlikely to fully account for the persistent summertime high MDA8 O_3 observed over northern natural

https://doi.org/10.1021/acs.est.6c06361
Environ. Sci. Technol. 2026, 60, 20484−20495

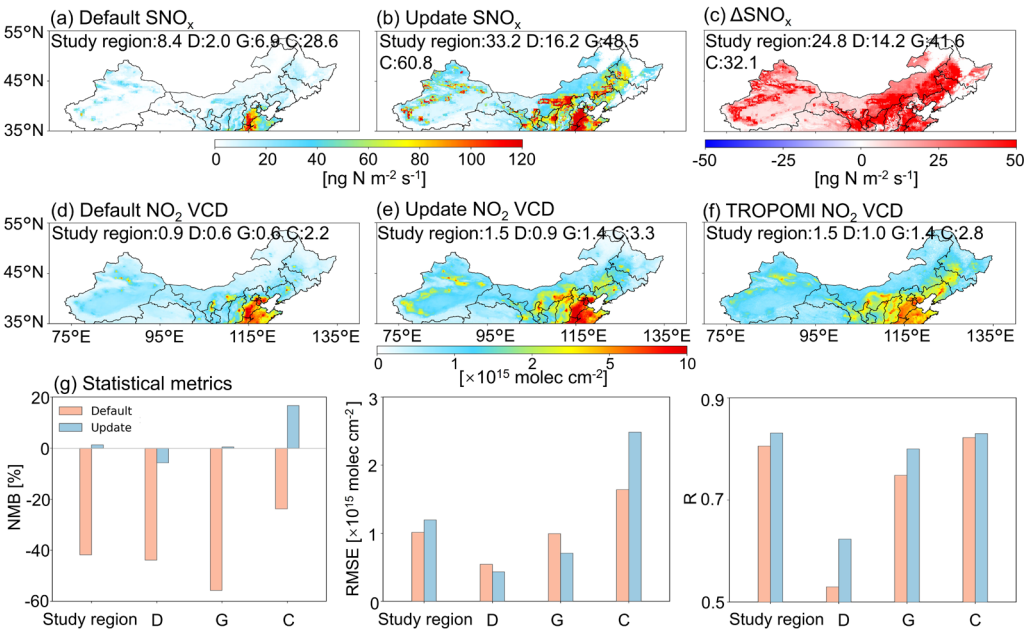

Figure 3. Spatial distributions of SNO_x and tropospheric NO_2 VCDs over North China in June 2022, together with statistical metrics for the simulated NO_2 VCDs. (a,b) Monthly mean SNO_x fluxes from the Default and Updated simulations, respectively. (c) Spatial differences in SNO_x between the two simulations (Update−Default). (d,e) Simulated tropospheric NO_2 VCDs from the Default and Updated simulations, respectively. (f) Tropospheric NO_2 VCDs from TROPOMI satellites. (g) Statistical metrics, including NMB, Root Mean Square Error (RMSE), and spatial correlation coefficients (R), for the simulated NO_2 VCDs across different land cover types. Statistics in panel (a−f) represent the mean values for the study region and three land cover types (D: Deserts, G: Grasslands, and C: Croplands).

background regions during 2018−2024. Moreover, despite differences in the summertime MDA8 O_3 trends derived from the CNEMC ground-based observations and CHAP fused data set, they both reveal a consistent increasing trend in MDA8 O_3 across major natural background regions in North China, particularly over grasslands (Figure S3c,d). These findings reveal that severe O_3 pollution is no longer confined to anthropogenic-dominated urban regions; natural background regions also exhibit notably high O_3 levels, which warrants more attention.

To elucidate the drivers of this spatial O_3 anomaly, we analyze the spatiotemporal trends of tropospheric NO_2 VCDs from TROPOMI satellites during the same period (Figures 2c and S3b). It shows that, although summer NO_2 VCDs in most urban areas and adjacent croplands are higher than in nonurban areas, these regions exhibit a general decreasing trend in NO_2 VCDs of -0.5×1014 molecules cm^{-2} yr^{-1} (-2.0% yr^{-1}). In contrast, natural backgrounds such as deserts and grasslands show a clear increasing trend, with a rise of $0.1-0.2 \times 10^{14}$ molecules cm^{-3} yr^{-1} (1.4%−2.3% yr^{-1}). Given that anthropogenic emissions are practically negligible in these remote backgrounds, the observed increase in NO_2 VCDs is primarily attributable to enhanced natural sources. This suggests that SNO_x play an indispensable role in O_3 formation over these regions. Furthermore, NO_2 VCDs over North China are markedly amplified under extreme dry-hot conditions (Figures 2d, S4). Under high-temperature conditions (T2 > 35 °C) and severe drought (soil moisture lower than 0.15 m^3 m^{-3}), the mean NO_2 VCDs exceed 1.2×10^{15} molecules cm^{-2}, with maximum values reaching 5.0×10^{15} molecules cm^{-2}, comparable to those observed in polluted urban regions. This compelling evidence demonstrates that changes in soil temperature and moisture under extreme climate events may regulate SNO_x, thus playing an important role in exacerbating O_3 pollution in background regions.

3.2. Improved Simulation Performance of the Optimized SNO_x Scheme

The summer of 2022 was characterized by one of the most severe compound heat and drought stresses recorded in China since 1961.[75] To investigate the specific impacts of CDHEs on SNO_x enhancement, we focus on June 2022, as this month recorded the highest occurrence frequency and broadest spatial extent of CDHEs across North China, peaking during an intense window from 13 to 22 June (Figure S5). Relative to the 2018−2024 climatology means for June, the regional $T2_{max}$ over North China during this period exhibited a positive anomaly of 1.3 °C (6.0%), coupled with soil moisture deficit by 0.005 m^3 m^{-3} (7.1%). These anomalies differ markedly across land cover types: grasslands recorded the highest $T2_{max}$ anomaly, reaching 1.5 °C (8.1%), while deserts showed the strongest drying signal, with soil moisture decreasing by about 23.9% (Figure S6). Driven by these extreme conditions, station-observed MDA8 O_3 concentrations at CNEMC sites rose significantly during the peak CDHE window: region-averaged O_3 levels increased by 6.1 μg m^{-3} relative to the 2018−2024 June climatological mean, and by an even more pronounced margin of 13.8 μg m^{-3} when compared to non-CDHE days within the same month (Figure S9). We further evaluate the model performance in reproducing these critical meteorological drivers (details in Text S4). Although the UI-WRF-Chem model tends to overestimate air temperature (both T2 and $T2_{max}$) and soil moisture, which may introduce uncertainties in SNO_x estimates, it nevertheless reasonably reproduces the spatiotemporal distribution of the extreme events.

We update soil temperature and moisture response functions ($f(T) \times g(\mathrm{WFPS})$) within the BDISNP scheme for three

https://doi.org/10.1021/acs.est.6c06361
Environ. Sci. Technol. 2026, 60, 20484−20495

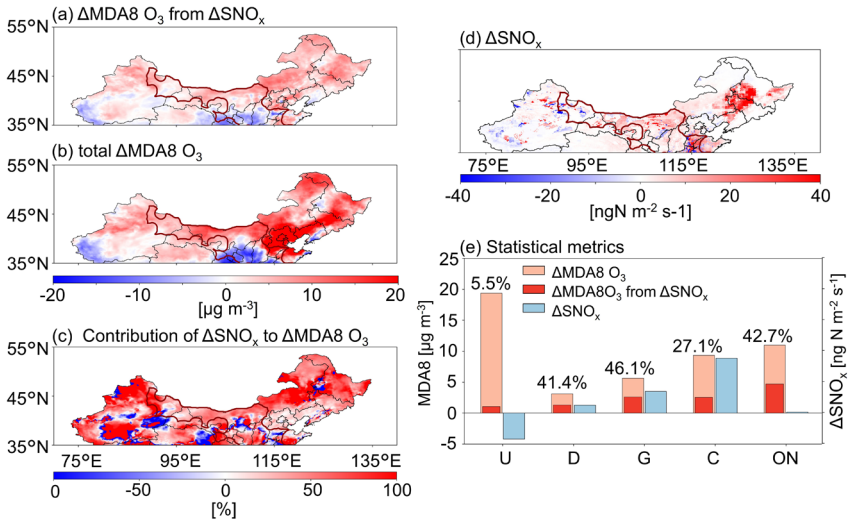

Figure 4. Spatial distributions of CDHE-induced SNO_x variations and their impacts on MDA8 O_3 concentrations over North China (June 2022). (a) SNO_x-driven changes in MDA8 O_3, derived from the difference between the Updated and NoSNOx simulations during CDHE relative to the non-CDHE periods. (b) Total CDHE-induced changes in MDA8 O_3 based on the Updated simulation. (c) Relative contribution of SNO_x to the total MDA8 O_3 changes (calculated as ΔMDA8 O_3 from SNO_x/total ΔMDA8 O_3). (d) Absolute variations in SNO_x between the CDHE and non-CDHE periods in the Updated simulation. (e) Statistics of the changes shown in (a−c) over different land cover types (U, D, G, C, and ON are the same as Figure 2).

major natural land cover types over North China: deserts, grasslands, and croplands. Because forests account for only 5.7% of the study domain and provide relatively limited samples within the CDHE-affected regions, we do not derive a forest-specific response function. As shown in Figure S10, the updated parametrization scheme substantially alters the SNO_x response to soil temperature and moisture across different land cover types, markedly enhancing the response factors under high-temperature conditions. The optimum WFPS driving peak emissions exhibits strong biome-dependence: peaking at a relatively low 27.0% for deserts, while shifting higher for grasslands (arid: 42.0%; nonarid: 49.0%) and croplands (arid: 29.0%; nonarid: 60.0%). The calibration leads to a substantial enhancement of simulated SNO_x fluxes over North China in June 2022 (Figure 3a−c). In the Updated simulation, the desert SNO_x flux reaches 16.2 ng N m^{-2} s^{-1} (8.2 times higher than that in the Default). Similarly, the simulated SNO_x fluxes over grasslands and croplands also increase by factors of 7.0 and 2.1, respectively. To evaluate the accuracy of these enhanced SNO_x estimates, we compiled available in situ SNO_x flux measurements from previously published studies (Table S4). As illustrated in Figure S11, the Updated simulation reasonably captures the observed order of magnitude and biome-specific variations of summer SNO_x fluxes in North China. Specifically, the only available field observations of desert SNO_x fluxes from Xinjiang province in China range from 2.8 to 7.9 ng N m^{-2} s^{-1}. Although our simulated fluxes (6.3 ∼25.6 ng N m^{-2} s^{-1}) slightly exceed these local measurements, they remain well within a reasonable range, as observations from other global deserts reported peck fluxes reaching several hundred ng N m^{-2} s^{-1}. Additionally, comparisons with field measurements at four grassland and cropland sites in North China reveal that the simulated mean SNO_x fluxes exhibit acceptable biases of −9.9 ∼39.2 and −54.9∼−22.6 ng N m^{-2} s^{-1}, respectively. We acknowledge, however, that the limited number of available field measurements restricts the robustness of a direct validation. Temporal mismatches between historical field measurement periods and our simulation year (2022) also contribute to the observed discrepancies.

To further validate the performance of the ML-derived SNO_x scheme, we compared the top-down SNO_x samples used for MoE model training against the simulated SNO_x fluxes in the Updated across varying soil temperature and moisture conditions (Figure S15). Although the Updated simulation effectively captures the overall SNO_x characteristics, specific discrepancies still show under certain regimes. In desert regions, the simulated SNO_x are generally lower than the training samples across all soil temperature and moisture ranges, with the bias of −75.6∼−18.4%. Conversely, over grasslands and croplands, the simulated SNO_x tend to exceed the training samples, specifically under extreme dry-hot conditions (soil temperature >30 °C and soil moisture <0.2 m^3 m^{-3}). A detailed discussion of the factors driving these biome- and regime-specific SNO_x discrepancies is provided in Text S7. Based on these evaluated SNO_x flux enhancements, the optimized scheme shifts the background NO_x budget toward a regime overwhelmingly dominated by natural sources during a representative CDHE month, with the SNO_x contribution increasing from 85.9% (Default) to 96.8% (Updated) in deserts, 74.3% to 92.0% in grasslands, and 55.6% to 72.5% in croplands (Figure S12).

We also evaluate the simulation performance of the UI-WRF-Chem model coupled with the optimized SNO_x scheme in simulating NO_2 during June 2022. The enhanced SNO_x fluxes lead to substantial improvements in simulated NO_2 VCDs over North China (Figures 3d−f and S13). Compared to TROPOMI observations (regional mean of 1.50 × 10^{15} molecules cm^{-2}), the Default simulations severely underestimate NO_2 VCDs (0.87 × 10^{15} molecules cm^{-2}), whereas the Updated simulations increase the simulated NO_2 VCDs to 1.51 × 10^{15} molecules cm^{-2}, effectively reducing the normalized mean bias (NMB) from −41.8% to 1.3%. Systemic improvements are clearly evident in both deserts and grasslands, with lower biases and higher spatial correlations of the simulated NO_2 VCDs, despite an overestimation being

https://doi.org/10.1021/acs.est.6c06361
Environ. Sci. Technol. 2026, 60, 20484−20495

found in croplands (Figure 3g). Moreover, the Updated simulation can successfully reproduce the observed NO_2 VCDs sensitivities to soil temperature and moisture variations over different land cover types (Figure S14). Under extreme dry-hot conditions (soil temperature >30 °C and soil moisture <0.15 m^3 m^{-3}), the Default simulation consistently underestimates NO_2 VCDs except in croplands, whereas the Updated simulation effectively reduces the NMB from −43.9% to −6.0% over deserts and from −55.5% to 0.7% over grasslands. However, the Updated simulation overestimates NO_2 VCDs over croplands, especially during high-temperature conditions, which may be attributed to uncertainties in the baseline nitrogen fertilizer application data and the bottom-up MEIC anthropogenic inventory used in the model. Nevertheless, comparisons with surface NO_2 observations also validate the improved performance of the Updated simulation (details in Text S5). These results confirm that the optimized SNO_x scheme not only improves the NO_2 simulation performance but also refines the representation of SNO_x-related physical processes affected by meteorological factors in the model.

3.3. CDHE Amplifies Ozone Pollution by Increasing SNO_x

Before analyzing the impact of CHDE-induced SNO_x on O_3 formation, we first evaluate the performance of the Updated simulation in reproducing MDA8 O_3 against CNEMC observations for June 2022. Although the model overestimates MDA8 O_3 by approximately 32.1% over North China, it successfully reproduces the spatial distribution of O_3 pollution, yielding a high R of 0.82 (Figure S16). Such overestimation of peak O_3 concentrations is a common challenge in current regional chemical transport models, which is typically attributed to uncertainties in precursor emissions, biases in vertical mixing and boundary-layer processes, and errors in dry deposition.[76−78]

To quantify the enhancement in surface MDA8 O_3 concentrations driven by CDHE-induced SNO_x across different land cover types, we compare the simulations from the CDHE period (13−22 June) against those from the non-CDHE baseline period (the remaining 20 days of June) (Figure 4). Our findings reveal that the enhanced SNO_x significantly exacerbates O_3 formations over natural regions in North China. Specifically, under CDHE conditions, desert SNO_x increase by only 1.3 ng N m^{-2} s^{-1}; it is worth noting that this modest flux increment contributes to 41.4% (1.3 μg m^{-3}) of the local total O_3 enhancements. Similarly, SNO_x over grasslands and other natural land cover types (ON) increase by 3.5 ng N m^{-2} s^{-1} and 0.16 ng N m^{-2} s^{-1}, respectively, driving 46.1% (2.6 μg m^{-3}) and 42.3% (4.7 μg m^{-3}) of the corresponding O_3 enhancements. In contrast, although croplands exhibit a considerable rise in SNO_x during CDHEs, with an increment of 8.9 ng N m^{-2} s^{-1}, the corresponding O_3 formation efficiency is relatively lower and only contributes 27.1% (2.5 μg m-3) to the total O_3 increases. In comparison, urban areas experience the most severe O_3 enhancements during CDHEs (19.4 μg m^{-3}), while the SNO_x contributions are negligible (5.5%, 1.1 μg m^{-3}). This suggests that variations in urban O_3 levels are predominantly controlled by other meteorology-regulated nonsoil NO_x emission processes.

The distinct spatial heterogeneity in SNO_x contribution to O_3 formation is primarily governed by the chemical sensitivity regime and O_3 formation efficiency. In natural regions, such as deserts and grasslands, low anthropogenic NO_x emissions and intense photochemical reactions create a strongly NO_x-limited regime. Accordingly, even moderate CDHE-induced increases in SNO_x can efficiently promote O_3 formation. In comparison, croplands and urban areas sustain much higher NO_x levels, where O_3 formation is dominated by transitional or VOCs-limited regimes and thus exhibits weaker sensitivity to changes in SNO_x.[79−82] Additionally, the extreme heat and strong solar radiation associated with CDHEs can accelerate soil emission flux and atmospheric nitrogen cycling over arid natural backgrounds. Coupled with high NO_x oxidation efficiency, the active photochemical reaction substantially elevates the potential for O_3 formation in these regions.[20] Overall, CDHEs not only directly regulate NO_x oxidation efficiency and O_3 photochemical reaction rate through meteorological forcing, but also increase soil emissions and accelerate regional nitrogen cycling, thereby enhancing the precursor supply in natural background regions. We highlight that accurate characterization of the nonlinear SNO_x response to soil temperature and moisture is essential for reliable O_3 pollution assessment and elucidating its driving mechanisms over natural regions during extreme climate events. Beyond these SNO_x-specific processes, climate-driven CDHEs also broadly exacerbate regional O_3 pollution through other mechanisms across both urban and natural landscapes, such as increasing biogenic volatile organic compound (BVOC) emissions,[21,83,84] and enhancing atmospheric oxidative capacity via accelerated nitrate photolysis and photoenhanced heterogeneous reactions.[85−87]

4. UNCERTAINTY ANALYSIS

We acknowledge the inherent uncertainties associated with the interpretable ML models used to update the soil temperature and moisture response functions. To assess the uncertainties associated with structure selection and parameter optimization, we defined a response factor, $\Phi = f(T) \times g(\mathrm{WFPS})$, that describes the combined influence of soil temperature and moisture on SNO_x. Structural robustness is evaluated through 30 independent training iterations utilizing randomized initializations and data partitions, with the dominant structures identified via final gating weights. The structure of the g(WFPS) demonstrates high stability across all iterations, indicating high identifiability. In contrast, candidate functions for $f(T)$ exhibits structural competition, suggesting limited discrimination among alternative functional forms (Figure S18a). Nevertheless, these structural variations show a negligible impact on the final magnitude of the simulated SNO_x responses. We also quantified the uncertainties arising from parameter optimization by calculating the corresponding Φ for each repeated training run. The fifth−95th percentile (P05−P95) interval across the ensemble of repeated training runs is used to characterize the intrinsic uncertainty introduced by training stochasticity and differences in sample partitioning, with the interval bounds expressed as percentage deviations relative to the median. Under standard constraints as the main experiment, the domain-weighted mean P05−P95 interval of Φ ranged from −0.4% to 0.4% relative to the median. Among land cover types, the parametric uncertainties are highest for croplands (−9.1% to 1.4%), moderate for grasslands (−4.2% to 2.0%), and negligible for deserts (−0.1% to 1.0%) (Figure S18b). Overall, methodological uncertainties could induce a maximum underestimation of 9.1% and an overestimation of 2.0% in simulated SNO_x. This confirms that the updated soil temperature and moisture response functions ($f(T)\cdot g$(WFPS)) are robust across the three natural land cover types. We also

https://doi.org/10.1021/acs.est.6c06361
Environ. Sci. Technol. 2026, 60, 20484−20495

quantify the relative importances of each fitted parameter within the final parametrization framework, and find that the updated SNO_x scheme is primarily governed by the intensity of the soil temperature response (a), soil temperature saturation threshold (T_{sat}), and peak-decay characteristics of the soil moisture response (k) (Figure S18c).

Uncertainties also remain in satellite observations and SNO_x inversion. First, uncertainties in satellite-retrieved tropospheric NO_2 VCDs arise primarily from the air-mass-factor and cloud-correction steps. These derivations depend on the treatment of cloud fraction and cloud pressure, surface albedo, aerosol loading, and viewing geometry. These factors can introduce systematic biases into the observed NO_2 VCDs, which subsequently propagate into the top-down SNO_x inversion.[34] The TROPOMI NO_2 products used in this study cover versions from v2.4.0 to v2.6.0; although the discrepancies between v2.4.0 and v2.5.0 are negligible, the v2.6.0 data used for 2024 may lead to some underestimation of NO_2 VCDs, which introduces additional uncertainty into the SNO_x inversions in 2024. Second, the top-down inversion of total NO_x emissions is sensitive to boundary layer height, the fixed effective NO_x lifetime, the assumed NO_2/NO_x conversion ratio, and the horizontal wind fields used to characterize transport. Uncertainties in these variables may propagate into the final SNO_x estimates. For example, adopting a constant NO_2/NO_x ratio of 0.76 may introduce biases over natural background regions,[88,89] where distinct photochemical regimes and sparse fresh NO_x emissions alter NO_2/NO_x partitioning relative to urban areas.[90,91] This constant ratio is applied uniformly across all years and land cover types; it thus impacts the absolute magnitude of the total NO_x inversion.[92] Third, isolating SNO_x samples from the top-down total NO_x emissions can introduce additional uncertainties. Despite implementing rigorous masking and correction procedures, residual uncertainties may arise from subgrid misclassification of land cover types induced by grid resampling (Text S6 for details) and the incomplete removal of background NO_x contributions from other natural sources, such as livestock grazing.[93,94] These unconstrained factors may inadvertently incorporate nonsoil signals into the satellite-derived SNO_x samples, thereby introducing moderate deviations into the biome-specific soil temperature-moisture response functions. Furthermore, inherent model biases in simulating extreme temperature and soil moisture may affect the accurate representation of SNO_x responses to soil temperature–moisture conditions. Fully constraining the spatiotemporal heterogeneity of available nitrogen pools, canopy reduction, and pulsing effects remains a persistent challenge that warrants further study.

5. IMPLICATIONS

The high summertime O_3 concentrations over natural background regions in North China are closely coupled with enhanced NO_2 VCDs, highlighting those natural emissions, specifically SNO_x, constitute a critical yet often overlooked driver of background O_3 pollution during extreme heat and drought. Utilizing the advanced, data-driven SNO_x scheme, our simulations demonstrate that CDHEs can substantially amplify SNO_x fluxes, accounting for nearly half of the regional O_3 increases. Consequently, SNO_x are not merely a relatively stable natural background source, but may instead act as an important driver of O_3 formation under extreme meteorological conditions, particularly in deserts and grasslands.

Climate change indirectly influences photochemistry by altering natural precursor supplies, establishing SNO_x as a dynamic feedback process highly sensitive to extreme events. However, current SNO_x schemes have distinct limitations in capturing soil temperature and moisture responses under dry-hot conditions. These parametrization biases may be further amplified during CDHEs, directly affecting the ability of atmospheric chemical transport models and climate models to simulate the impacts of natural emissions on O_3 anomalies. Future model development should thus improve their representation of SNO_x under extreme climate events, focusing on continuous high-temperature response, low soil moisture suppression thresholds, and the short-term enhancement following precipitation and irrigation pulses. Developing observation-constrained parametrization schemes by specific land covers is also a critical necessity for accurately representing the climate sensitivity of O_3 pollution. Additionally, long-term field SNO_x flux observations and controlled experiments are required to constrain the dynamic emission responses to the combined effects of soil temperature and moisture, especially in extreme dry-hot conditions. The relative contributions of nitrification, denitrification, and associated microbial processes to SNO_x during extreme climate events should be clearly disentangled. To complement these ground-based efforts, the future integration of hourly observations from geostationary satellites, such as the Geostationary Environment Monitoring Spectrometer (GEMS), could further refine the diurnal dynamics of SNO_x. Incorporating observation-constrained SNO_x schemes into modeling frameworks will enable more reliable assessments of SNO_x contributions to interannual O_3 variability.

Ultimately, our findings in North China offer a critical global proxy. Across other arid and semiarid ecosystems worldwide, the climate-driven intensification of natural NO_x sources, especially SNO_x, is likely a widespread determinant of background O_3 anomalies. This climate-biosphere-chemistry feedback should therefore be systematically considered in future air-quality prediction and climate-adaptive management frameworks.

■ ASSOCIATED CONTENT

Data Availability Statement

The Level 2 TROPOMI NO_2 VCD_s were downloaded from NASA GES DISC (https://disc.gsfc.nasa.gov). Fire activities, soil temperature and soil moisture, and land cover types of data were obtained from the NASA FIRMS product, the NASA SMAP Level 4 soil product, and the MODIS MCD12C1 product, respectively (https://www.earthdata.nasa.gov/). Meteorological fields were obtained from the ECMWF ERA5 reanalysis data set (https://cds.climate.copernicus.eu/). The MEIC anthropogenic emission inventory was obtained from Tsinghua University (http://meicmodel.org.cn/). The gridded surface MDA8 O_3 over China was obtained from the CHAP data set published by Wei et al. (2022) (https://zenodo.org/communities/chap/). Agricultural fertilizer data were obtained from the China Statistical Yearbook (https://www.stats.gov.cn/sj/ndsj/). Atmospheric nitrogen deposition data were taken from the data set published by Gao et al. (2023) (10.6084/m9.figshare.24057120). Ground-based MDA8 O_3, hourly NO_2, and meteorological observations used for model evaluation were obtained from the China National Environmental

https://doi.org/10.1021/acs.est.6c06361
Environ. Sci. Technol. 2026, 60, 20484−20495

Monitoring Centre (http://www.cnemc.cn/) and China Meteorological Data Service Center (http://data.cma.cn/).

Supporting Information

The Supporting Information is available free of charge at https://pubs.acs.org/doi/10.1021/acs.est.6c06361.

Top-down total NO_x emissions inversion (Text S1); interannual calibration factor (Text S2); function libraries and ML optimization protocols (Text S3); meteorological variables (Text S4) and surface NO_2 and NO_x model evaluations (Text S5); subgrid land cover misclassification impacts (Text S6); drivers of training vs simulated SNO_x discrepancies (Text S7); nitrogen deposition and fertilizer application trends (Figure S1); soil nitrogen inputs interannual correction (Figure S2); summertime O_3 and NO_2 trends (Figure S3); NO_2 VCDs variations with air temperature and soil moisture (Figure S4); CDHE frequencies in summer 2022 (Figure S5); $T2_{max}$ and soil moisture anomalies (Figure S6); T2 and $T2_{max}$ model evaluations (Figure S7); SMAP and simulated soil moisture and temperature comparison (Figure S8); observed MDA8 O_3 anomalies (Figure S9); soil temperature−moisture response functions (Figure S10); simulated SNO_x vs field measurements (Figure S11); SNO_x contribution to total NO_x (Figure S12); simulated NO_2 VCDs bias (Figure S13); NO_2 VCDs variations across soil temperature and moisture regimes (Figure S14); simulated vs training SNO_x (Figure S15); MDA8 O_3 model evaluations (Figure S16); diurnal surface NO_2 and NO_x (Figure S17); response functions uncertainties (Figure S18); edge grids distributions (Figure S19); model experiment description (Table S1); soil porosity for Noah land surface model (Table S2); updated soil temperature−moisture response functions parameters (Table S3); and SNO_x field measurements (Table S4) (PDF)

AUTHOR INFORMATION

Corresponding Author

Tong Sha − *Shaanxi University Key Laboratory of Industrial Pollution Control and Environmental Health, School of Environmental Science and Engineering, Shaanxi University of Science & Technology, Xi'an 710021, China;* orcid.org/0000-0002-6490-387X; Email: tong-sha@sust.edu.cn

Authors

Zhao Yang − *Shaanxi University Key Laboratory of Industrial Pollution Control and Environmental Health, School of Environmental Science and Engineering, Shaanxi University of Science & Technology, Xi'an 710021, China*

Feng Wu − *State Key Laboratory of Loess Science, Institute of Earth Environment, Chinese Academy of Sciences, Xi'an 710061, China;* orcid.org/0000-0002-9570-5817

Qingcai Chen − *Shaanxi University Key Laboratory of Industrial Pollution Control and Environmental Health, School of Environmental Science and Engineering, Shaanxi University of Science & Technology, Xi'an 710021, China;* orcid.org/0000-0001-7450-0073

K. Folkert Boersma − *Satellite Observations Department, Royal Netherlands Meteorological Institute, De Bilt 3731 GA, The Netherlands; Meteorology and Air Quality Group, Wageningen University, Wageningen 6708 PB, The Netherlands;* orcid.org/0000-0002-4591-7635

Jun Wang − *Department of Chemical and Biochemical Engineering, Center for Global and Regional Environmental Research, and Iowa Technology Institute, University of Iowa, Iowa City, Iowa 52242, United States;* orcid.org/0000-0002-7334-0490

Yan-Lin Zhang − *School of Ecology and Applied Meteorology and Atmospheric Environment Center, Joint Laboratory for International Cooperation on Climate and Environmental Change, Ministry of Education (ILCEC), Nanjing University of Information Science & Technology, Nanjing 210044, China*

Complete contact information is available at: https://pubs.acs.org/10.1021/acs.est.6c06361

Author Contributions

[▽]Z.Y. and T.S. contributed equally to this work.

Notes

The authors declare no competing financial interest.

ACKNOWLEDGMENTS

This study is supported by the National Natural Science Foundation of China (grant nos. 42205107, 41971150). J.W.'s participation is made possible by the in-kind support (Lichtenberger Family Chair professorship) from the University of Iowa.

REFERENCES

(1) Delaria, E. R.; Cohen, R. C. Measurements of Atmosphere-Biosphere Exchange of Oxidized Nitrogen and Implications for the Chemistry of Atmospheric NO_x. *Acc. Chem. Res.* **2023**, *56* (13), 1720−1730.

(2) Sha, T.; Yang, S.; Chen, Q.; Li, L.; Ma, X.; Zhang, Y.-L.; Feng, Z.; Boersma, K. F.; Wang, J. Large contributions of soil emissions to the atmospheric nitrogen budget and their impacts on air quality and temperature rise in North China. *Atmos. Chem. Phys.* **2024**, *24* (14), 8441−8455.

(3) Lu, X.; Ye, X.; Zhou, M.; Zhao, Y.; Weng, H.; Kong, H.; Li, K.; Gao, M.; Zheng, B.; Lin, J.; et al. The underappreciated role of agricultural soil nitrogen oxide emissions in ozone pollution regulation in North China. *Nat. Commun.* **2021**, *12* (1), 5021.

(4) Elshorbany, Y.; Ziemke, J. R.; Strode, S.; Petetin, H.; Miyazaki, K.; De Smedt, I.; Pickering, K.; Seguel, R. J.; Worden, H.; Emmerichs, T.; et al. Tropospheric ozone precursors: global and regional distributions, trends, and variability. *Atmos. Chem. Phys.* **2024**, *24* (21), 12225−12257.

(5) Huber, D. E.; Kort, E. A.; Steiner, A. L. Soil moisture, soil NO_x and regional air quality in the agricultural central United States. *J. Geophys. Res.:Atmos.* **2024**, *129* (12), No. e2024JD041015.

(6) Li, J.; Zhang, Y.; Bevacqua, E.; Zscheischler, J.; Keenan, T. F.; Lian, X.; Zhou, S.; Zhang, H.; He, M.; Piao, S. Future increase in compound soil drought-heat extremes exacerbated by vegetation greening. *Nat. Commun.* **2024**, *15* (1), 10875.

(7) Zhang, B.; Wang, S.; Slater, L. Anthropogenic climate change doubled the frequency of compound drought and heatwaves in low-income regions. *Commun. Earth Environ.* **2024**, *5* (1), 715.

(8) Romer, P. S.; Duffey, K. C.; Wooldridge, P. J.; Edgerton, E.; Baumann, K.; Feiner, P. A.; Miller, D. O.; Brune, W. H.; Koss, A. R.; de Gouw, J. A.; et al. Effects of temperature-dependent NO_x emissions on continental ozone production. *Atmos. Chem. Phys.* **2018**, *18* (4), 2601−2614.

(9) Sha, T.; Ma, X.; Zhang, H.; Janechek, N.; Wang, Y.; Wang, Y.; Castro García, L.; Jenerette, G. D.; Wang, J. Impacts of Soil NO_x

Emission on O_3 Air Quality in Rural California. *Environ. Sci. Technol.* **2021**, *55* (10), 7113−7122.
(10) Wang, Y.; Li, Q.; Wang, Y.; Ren, C.; Saiz-Lopez, A.; Xue, L.; Wang, T. Increasing soil nitrous acid emissions driven by climate and fertilization change aggravate global ozone pollution. *Nat. Commun.* **2025**, *16* (1), 2463.
(11) Ren, C.; Huang, X.; Wang, Y.; Zhang, L.; Zhou, X.; Sun, W.; Zhang, H.; Liu, T.; Ding, A.; Wang, T. Enhanced soil emissions of reactive nitrogen gases by fertilization and their impacts on secondary air pollution in eastern China. *Environ. Sci. Technol.* **2025**, *59* (10), 5119−5130.
(12) Duan, R.; Huang, G.; Wang, F.; Tian, C.; Wu, X. Observations over a century underscore an increasing likelihood of compound dry-hot events in China. *Earth's Future* **2024**, *12* (11), No. e2024EF004546.
(13) Liang, Y.; Wang, J.; Hao, Z.; Wang, H.; Cui, H.; Ge, Q. Anthropogenically-driven escalating impact of soil-based compound dry-hot extremes on vegetation productivity. *Nat. Commun.* **2026**, *17*, 2303.
(14) Pan, X.; Wang, W.; Shao, Q.; Wei, J.; Li, H.; Zhang, F.; Cao, M.; Yang, L. Compound drought and heat waves variation and association with SST modes across China. *Sci. Total Environ.* **2024**, *907*, 167934.
(15) Hu, Y.; Wang, W.; Wang, P.; Teuling, A. J.; Zhu, Y. Spatial-temporal variations and drivers of the compound dry-hot event in China. *Atmos. Res.* **2024**, *299*, 107160.
(16) McCalley, C. K.; Sparks, J. P. Abiotic Gas Formation Drives Nitrogen Loss from a Desert Ecosystem. *Sci.* **2009**, *326* (5954), 837−840.
(17) Georgiou, C. D.; Sun, H. J.; McKay, C. P.; Grintzalis, K.; Papapostolou, I.; Zisimopoulos, D.; Panagiotidis, K.; Zhang, G.; Koutsopoulou, E.; Christidis, G. E.; et al. Evidence for photochemical production of reactive oxygen species in desert soils. *Nat. Commun.* **2015**, *6* (1), 7100.
(18) Wang, B.; Lee, X.; Theng, B. K. G.; Cheng, J.; Yang, F. Diurnal and spatial variations of soil NO_x fluxes in the northern steppe of China. *J. Environ. Sci.* **2015**, *32*, 54−61.
(19) Weber, B.; Wu, D.; Tamm, A.; Ruckteschler, N.; Rodriguez-Caballero, E.; Steinkamp, J.; Meusel, H.; Elbert, W.; Behrendt, T.; Sörgel, M.; et al. Biological soil crusts accelerate the nitrogen cycle through large NO and HONO emissions in drylands. *Proc. Natl. Acad. Sci. U. S. A.* **2015**, *112* (50), 15384−15389.
(20) Wu, F.; Hu, T.; Cao, J.; Guo, X.; Li, G.; Zhang, T.; Yang, Y.; Zhao, C.; Zhang, D. Active nitrogen cycle driven by solar radiation in clean desert air. *Earth's Future* **2022**, *10* (4), No. e2021EF002451.
(21) Wang, Y.; Wang, Y.; Li, Q.; Chen, T.; Tan, Y.; Wang, T. Synergy of Natural Sources Exacerbates Ozone Pollution in China during Drought-Heatwave Extremes. *Environ. Sci. Technol.* **2025**, *59* (42), 22739−22748.
(22) Hudman, R. C.; Moore, N. E.; Mebust, A. K.; Martin, R. V.; Russell, A. R.; Valin, L. C.; Cohen, R. C. Steps towards a mechanistic model of global soil nitric oxide emissions: implementation and space based-constraints. *Atmos. Chem. Phys.* **2012**, *12* (16), 7779−7795.
(23) Yienger, J. J.; Levy II, H. Empirical model of global soil-biogenic NO_x emissions. *J. Geophys. Res.:Atmos.* **1995**, *100* (D6), 11447−11464.
(24) Wang, Y.; Ge, C.; Castro, L.; Jenerette, G.; Oikawa, P.; Wang, J. Improved modelling of soil NO_x emissions in a high temperature agricultural region: role of background emissions on NO_2 trend over the US. *Environ. Res. Lett.* **2021**, *16*, 084061.
(25) Schindlbacher, A.; Zechmeister-Boltenstern, S.; Butterbach-Bahl, K. Effects of soil moisture and temperature on NO, NO_2, and N_2O emissions from European forest soils. *J. Geophys. Res.:Atmos.* **2004**, *109* (D17), D17302.
(26) Sha, T.; Ma, X.; Zhang, H.; Janechek, N.; Wang, Y.; Wang, Y.; Castro García, L.; Jenerette, G. D.; Wang, J. Impacts of soil NO_x emission on O_3 air quality in rural California. *Environ. Sci. Technol.* **2021**, *55* (10), 7113−7122.
(27) Rasool, Q. Z.; Zhang, R.; Lash, B.; Cohan, D. S.; Cooter, E. J.; Bash, J. O.; Lamsal, L. N. Enhanced representation of soil NO emissions in the Community Multiscale Air Quality (CMAQ) model version 5.0. 2. *Geosci. Model Dev.* **2016**, *9* (9), 3177−3197.
(28) Huber, D. E.; Steiner, A. L.; Kort, E. A. Sensitivity of modeled soil NO_x emissions to soil moisture. *J. Geophys. Res.:Atmos.* **2023**, *128* (7), No. e2022JD037611.
(29) Huber, D. E.; Kerr, G. H.; Nawaz, M. O.; Runkel, S.; Anenberg, S. C.; Goldberg, D. L. Global NO_2 changes between 2019 and 2024 as observed by TROPOMI in urban areas and emerging hotspots. *Atmos. Chem. Phys.* **2026**, *26* (5), 3783−3803.
(30) Omrani, H.; Omrani, B.; Parmentier, B.; Helbich, M. Spatio-temporal data on the air pollutant nitrogen dioxide derived from Sentinel satellite for France. *Data Brief* **2020**, *28*, 105089.
(31) Johnson, M. S.; Philip, S.; Kumar, R.; Naeger, A.; Souri, A. H.; Geddes, J.; Judd, L.; Janz, S.; Sullivan, J. Satellite remote-sensing capability to assess tropospheric-column ratios of formaldehyde and nitrogen dioxide: case study during the Long Island Sound Tropospheric Ozone Study 2018 (LISTOS 2018) field campaign. *Atmos. Meas. Tech.* **2022**, *16*, 2431−2454.
(32) Zhao, X.; Griffin, D.; Fioletov, V.; McLinden, C.; Cede, A.; Tiefengraber, M.; Müller, M.; Bognar, K.; Strong, K.; Boersma, F.; et al. Assessment of the quality of TROPOMI high-spatial-resolution NO_2 data products in the Greater Toronto Area. *Atmos. Meas. Tech.* **2020**, *13* (4), 2131−2159.
(33) Lange, K.; Richter, A.; Schönhardt, A.; Meier, A. C.; Bösch, T.; Seyler, A.; Krause, K.; Behrens, L. K.; Wittrock, F.; Merlaud, A.; et al. Validation of Sentinel-5P TROPOMI tropospheric NO_2 products by comparison with NO_2 measurements from airborne imaging DOAS, ground-based stationary DOAS, and mobile car DOAS measurements during the S5P-VAL-DE-Ruhr campaign. *Atmos. Meas. Tech.* **2023**, *16* (5), 1357−1389.
(34) Van Geffen, J.; Eskes, H.; Compernolle, S.; Pinardi, G.; Verhoelst, T.; Lambert, J.-C.; Sneep, M.; Ter Linden, M.; Ludewig, A.; Boersma, K. F.; et al. Sentinel-5P TROPOMI NO_2 retrieval: impact of version v2. 2 improvements and comparisons with OMI and ground-based data. *Atmos. Meas. Tech.* **2022**, *15* (7), 2037−2060.
(35) Hersbach, H.; Bell, B.; Berrisford, P.; Hirahara, S.; Horányi, A.; Muñoz-Sabater, J.; Nicolas, J.; Peubey, C.; Radu, R.; Schepers, D.; et al. The ERA5 global reanalysis. *Q. J. R. Meteorol. Soc.* **2020**, *146* (730), 1999−2049.
(36) Muñoz-Sabater, J.; Dutra, E.; Agustí-Panareda, A.; Albergel, C.; Arduini, G.; Balsamo, G.; Boussetta, S.; Choulga, M.; Harrigan, S.; Hersbach, H.; et al. ERA5-Land: a state-of-the-art global reanalysis dataset for land applications. *Earth Syst. Sci. Data* **2021**, *13* (9), 4349−4383.
(37) Sulla-Menashe, D.; Friedl, M. *MODIS Collection 6.1 (C61) land cover type product user guide*; United States Geological Survey: Reston, VA, USA, 2022.
(38) Sulla-Menashe, D.; Gray, J. M.; Abercrombie, S. P.; Friedl, M. A. Hierarchical mapping of annual global land cover 2001 to present: The MODIS Collection 6 Land Cover product. *Remote Sens. Environ.* **2019**, *222*, 183−194.
(39) Gao, Q.; Zhang, X.; Liu, L.; Lu, X.; Wang, Y. A database of atmospheric inorganic nitrogen deposition fluxes in China from satellite monitoring. *Sci. Data* **2023**, *10* (1), 698.
(40) Wei, J.; Li, Z.; Li, K.; Dickerson, R. R.; Pinker, R. T.; Wang, J.; Liu, X.; Sun, L.; Xue, W.; Cribb, M. Full-coverage mapping and spatiotemporal variations of ground-level ozone (O_3) pollution from 2013 to 2020 across China. *Remote Sens. Environ.* **2022**, *270*, 112775.
(41) Grell, G. A.; Peckham, S. E.; Schmitz, R.; McKeen, S. A.; Frost, G.; Skamarock, W. C.; Eder, B. Fully coupled "online" chemistry within the WRF model. *Atmos. Environ.* **2005**, *39* (37), 6957−6975.
(42) Zhang, H.; Wang, J.; Janechek, N.; Ge, C.; Zhou, M.; Castro García, L.; Sha, T.; Wang, Y.; Deng, W.; Xue, Z.; et al. Development of UI-WRF-Chem (v1. 0) for the MAIA satellite mission: case demonstration. *Geosci. Model Dev.* **2025**, *18* (22), 9061−9099.
(43) Gelaro, R.; McCarty, W.; Suárez, M. J.; Todling, R.; Molod, A.; Takacs, L.; Randles, C. A.; Darmenov, A.; Bosilovich, M. G.; Reichle,

R.; et al. The modern-era retrospective analysis for research and applications, version 2 (MERRA-2). *J. Clim.* **2017**, *30* (14), 5419−5454.
(44) Rodell, M.; Houser, P.; Jambor, U.; Gottschalck, J.; Mitchell, K.; Meng, C.-J.; Arsenault, K.; Cosgrove, B.; Radakovich, J.; Bosilovich, M.; et al. The global land data assimilation system. *Bull. Am. Meteorol. Soc.* **2004**, *85* (3), 381−394.
(45) Wiedinmyer, C.; Akagi, S.; Yokelson, R. J.; Emmons, L.; Al-Saadi, J.; Orlando, J.; Soja, A. The Fire INventory from NCAR (FINN): A high resolution global model to estimate the emissions from open burning. *Geosci. Model Dev.* **2011**, *4* (3), 625−641.
(46) Guenther, A.; Jiang, X.; Heald, C. L.; Sakulyanontvittaya, T.; Duhl, T. a.; Emmons, L.; Wang, X. The Model of Emissions of Gases and Aerosols from Nature version 2.1 (MEGAN2. 1): an extended and updated framework for modeling biogenic emissions. *Geosci. Model Dev.* **2012**, *5* (6), 1471−1492.
(47) Morrison, H.; Thompson, G.; Tatarskii, V. Impact of cloud microphysics on the development of trailing stratiform precipitation in a simulated squall line: Comparison of one-and two-moment schemes. *Mon. Weather Rev.* **2009**, *137* (3), 991−1007.
(48) Grell, G. A.; Dévényi, D. A generalized approach to parameterizing convection combining ensemble and data assimilation techniques. *Geophys. Res. Lett.* **2002**, *29* (14), 38−31−38−34.
(49) Iacono, M. J.; Delamere, J. S.; Mlawer, E. J.; Shephard, M. W.; Clough, S. A.; Collins, W. D. Radiative forcing by long-lived greenhouse gases: Calculations with the AER radiative transfer models. *J. Geophys. Res.:Atmos.* **2008**, *113* (D13), D13103.
(50) Cheng, F.-Y.; Chin, S.-C.; Liu, T.-H. The role of boundary layer schemes in meteorological and air quality simulations of the Taiwan area. *Atmos. Environ.* **2012**, *54*, 714−727.
(51) Tewari, M.; Chen, F.; Wang, W.; Dudhia, J.; LeMone, M. A.; Mitchell, K.; Ek, M.; Gayno, G.; Wegiel, J.; Cuenca, R. H. Implementation and Verification of the Unified Noah Land Surface Model in the WRF Model. In *Preprints, 20th Conference on Weather Analysis and Forecasting/16th Conference on Numerical Weather Prediction*; American Meteorological Society: Seattle, WA, 2004; Paper 14A.2.
(52) Stockwell, W. R.; Middleton, P.; Chang, J. S.; Tang, X. The second generation regional acid deposition model chemical mechanism for regional air quality modeling. *J. Geophys. Res.:Atmos.* **1990**, *95* (D10), 16343−16367.
(53) Schell, B.; Ackermann, I. J.; Hass, H.; Binkowski, F. S.; Ebel, A. Modeling the formation of secondary organic aerosol within a comprehensive air quality model system. *J. Geophys. Res.:Atmos.* **2001**, *106* (D22), 28275−28293.
(54) Ackermann, I. J.; Hass, H.; Memmesheimer, M.; Ebel, A.; Binkowski, F. S.; Shankar, U. Modal aerosol dynamics model for Europe: Development and first applications. *Atmos. Environ.* **1998**, *32* (17), 2981−2999.
(55) Kong, H.; Lin, J.; Chen, L.; Zhang, Y.; Yan, Y.; Liu, M.; Ni, R.; Liu, Z.; Weng, H. Considerable unaccounted local sources of NO_x emissions in China revealed from satellite. *Environ. Sci. Technol.* **2022**, *56* (11), 7131−7142.
(56) Hudman, R.; Moore, N.; Mebust, A.; Martin, R.; Russell, A.; Valin, L.; Cohen, R. Steps towards a mechanistic model of global soil nitric oxide emissions: implementation and space based-constraints. *Atmos. Chem. Phys.* **2012**, *12* (16), 7779−7795.
(57) Hickman, J. E.; Dammers, E.; Galy-Lacaux, C.; Van der Werf, G. R. Satellite evidence of substantial rain-induced soil emissions of ammonia across the Sahel. *Atmos. Chem. Phys.* **2018**, *18* (22), 16713−16727.
(58) Rasool, Q. Z.; Bash, J. O.; Cohan, D. S. Mechanistic representation of soil nitrogen emissions in the Community Multiscale Air Quality (CMAQ) model v 5.1. *Geosci. Model Dev.* **2019**, *12* (2), 849−878.
(59) Zörner, J.; Penning de Vries, M.; Beirle, S.; Sihler, H.; Veres, P. R.; Williams, J.; Wagner, T. Multi-satellite sensor study on precipitation-induced emission pulses of NO_x from soils in semi-arid ecosystems. *Atmos. Chem. Phys.* **2016**, *16* (14), 9457−9487.
(60) Szukics, U.; Abell, G. C.; Hödl, V.; Mitter, B.; Sessitsch, A.; Hackl, E.; Zechmeister-Boltenstern, S. Nitrifiers and denitrifiers respond rapidly to changed moisture and increasing temperature in a pristine forest soil. *FEMS Microbiol. Ecol.* **2010**, *72* (3), 395−406.
(61) Hazimeh, H.; Zhao, Z.; Chowdhery, A.; Sathiamoorthy, M.; Chen, Y.; Mazumder, R.; Hong, L.; Chi, E. Dselect-k: Differentiable selection in the mixture of experts with applications to multi-task learning. *NIPS'21: Proceedings of the 35th International Conference on Neural Information Processing Systems*, 2021; pp 29335−29347.
(62) Masoudnia, S.; Ebrahimpour, R. Mixture of experts: a literature survey. *Artif. Intell. Rev.* **2014**, *42* (2), 275−293.
(63) Jacobs, R. A.; Jordan, M. I.; Nowlan, S. J.; Hinton, G. E. Adaptive mixtures of local experts. *Neural Comput.* **1991**, *3* (1), 79−87.
(64) Delon, C.; Serça, D.; Boissard, C.; Dupont, R.; Dutot, A.; Laville, P.; De Rosnay, P.; Delmas, R. Soil NO emissions modelling using artificial neural network. *Tellus, Ser. B: Chem. Phys. Meteorol.* **2022**, *59* (3), 502−513.
(65) Weng, H.; Lin, J.; Martin, R.; Millet, D. B.; Jaeglé, L.; Ridley, D.; Keller, C.; Li, C.; Du, M.; Meng, J. Global high-resolution emissions of soil NO_x, sea salt aerosols, and biogenic volatile organic compounds. *Sci. Data* **2020**, *7* (1), 148.
(66) Taylor, A. E.; Giguere, A. T.; Zoebelein, C. M.; Myrold, D. D.; Bottomley, P. J. Modeling of soil nitrification responses to temperature reveals thermodynamic differences between ammonia-oxidizing activity of archaea and bacteria. *ISME J.* **2017**, *11* (4), 896−908.
(67) Hosseinzadehtalaei, P.; Termonia, P.; Tabari, H. Projected changes in compound hot-dry events depend on the dry indicator considered. *Commun. Earth Environ.* **2024**, *5* (1), 220.
(68) Weynants, M.; Ji, C.; Linscheid, N.; Weber, U.; Mahecha, M. D.; Gans, F. Dheed: an ERA5 based global database of compound dry and hot extreme events from 1950 to 2023. *Earth Syst. Sci. Data* **2025**, *17* (11), 6621−6645.
(69) Fan, X.; Zhang, Y.; Shi, K.; Peng, J.; Liu, Y.; Zhou, Y.; Liu, Y.; Zhu, Q.; Song, C.; Wan, R.; et al. Surging compound drought-heatwaves underrated in global soils. *Proc. Natl. Acad. Sci. U. S. A.* **2024**, *121* (42), No. e2410294121.
(70) Mukherjee, S.; Mishra, A. K.; Zscheischler, J.; Entekhabi, D. Interaction between dry and hot extremes at a global scale using a cascade modeling framework. *Nat. Commun.* **2023**, *14* (1), 277.
(71) Knowland, K.; Ott, L.; Duncan, B.; Wargan, K. Stratospheric intrusion-influenced ozone air quality exceedances investigated in the NASA MERRA-2 reanalysis. *Geophys. Res. Lett.* **2017**, *44* (20), 10691−10701.
(72) Fadnavis, S.; Chakraborty, T.; Beig, G. Seasonal Stratospheric Intrusion of Ozone in the Upper Troposphere over India. *Ann. Geophys.* **2010**, *28*, 2149−2159.
(73) Chen, Z.; Liu, J.; Qie, X.; Cheng, X.; Yang, M.; Shu, L.; Zang, Z. Stratospheric influence on surface ozone pollution in China. *Nat. Commun.* **2024**, *15* (1), 4064.
(74) Zhao, K.; Huang, J.; Wu, Y.; Yuan, Z.; Wang, Y.; Li, Y.; Ma, X.; Liu, X.; Ma, W.; Wang, Y.; et al. Impact of Stratospheric Intrusions on Ozone Enhancement in the Lower Troposphere and Implication to Air Quality in Hong Kong and Other South China Regions. *J. Geophys. Res.:Atmos.* **2021**, *126* (18), No. e2020JD033955.
(75) Wang, L.; Sun, L.; Li, W.; Chen, X.; Li, Y.; Zou, X.; Jiang, Y. State of China's climate in 2022. *Atmos. Oceanic Sci. Lett.* **2023**, *16* (6), 100356.
(76) Travis, K. R.; Jacob, D. J.; Fisher, J. A.; Kim, P. S.; Marais, E. A.; Zhu, L.; Yu, K.; Miller, C. C.; Yantosca, R. M.; Sulprizio, M. P.; et al. Why do models overestimate surface ozone in the Southeast United States? *Atmos. Chem. Phys.* **2016**, *16* (21), 13561−13577.
(77) Travis, K. R.; Jacob, D. J. Systematic bias in evaluating chemical transport models with maximum daily 8 h average (MDA8) surface ozone for air quality applications: a case study with GEOS-Chem v9.02. *Geosci. Model Dev.* **2019**, *12* (8), 3641−3648.
(78) Ye, X.; Wang, X.; Zhang, L. Diagnosing the Model Bias in Simulating Daily Surface Ozone Variability Using a Machine Learning

Method: The Effects of Dry Deposition and Cloud Optical Depth. *Environ. Sci. Technol.* **2022**, *56* (23), 16665−16675.
(79) Dahlmann, K.; Grewe, V.; Ponater, M.; Matthes, S. Quantifying the contributions of individual NO_x sources to the trend in ozone radiative forcing. *Atmos. Environ.* **2011**, *45* (17), 2860−2868.
(80) Lu, X.; Ye, X.; Zhou, M.; Zhao, Y.; Weng, H.; Kong, H.; Li, K.; Gao, M.; Zheng, B.; Lin, J.; et al. The underappreciated role of agricultural soil nitrogen oxide emissions in ozone pollution regulation in North China. *Nat. Commun.* **2021**, *12* (1), 5021.
(81) Ren, J.; Guo, F.; Xie, S. Diagnosing ozone-NO_x-VOC sensitivity and revealing causes of ozone increases in China based on 2013−2021 satellite retrievals. *Atmos. Chem. Phys.* **2022**, *22* (22), 15035−15047.
(82) Wang, W.; van der A, R.; Ding, J.; van Weele, M.; Cheng, T. Spatial and temporal changes of the ozone sensitivity in China based on satellite and ground-based observations. *Atmos. Chem. Phys.* **2021**, *21* (9), 7253−7269.
(83) Wang, H.; Wu, K.; Liu, Y.; Sheng, B.; Lu, X.; He, Y.; Xie, J.; Wang, H.; Fan, S. Role of Heat Wave-Induced Biogenic VOC Enhancements in Persistent Ozone Episodes Formation in Pearl River Delta. *J. Geophys. Res.:Atmos.* **2021**, *126* (12), No. e2020JD034317.
(84) Cao, J.; Situ, S.; Hao, Y.; Xie, S.; Li, L. Enhanced summertime ozone and SOA from biogenic volatile organic compound (BVOC) emissions due to vegetation biomass variability during 1981−2018 in China. *Atmos. Chem. Phys.* **2022**, *22* (4), 2351−2364.
(85) Ma, J.; Liu, Y.; Han, C.; Ma, Q.; Liu, C.; He, H. Review of heterogeneous photochemical reactions of NO_y on aerosol—A possible daytime source of nitrous acid (HONO) in the atmosphere. *J. Environ. Sci.* **2013**, *25* (2), 326−334.
(86) George, C.; Ammann, M.; D'Anna, B.; Donaldson, D.; Nizkorodov, S. A. Heterogeneous photochemistry in the atmosphere. *Chem. Rev.* **2015**, *115* (10), 4218−4258.
(87) Shah, V.; Keller, C. A.; Knowland, K. E.; Christiansen, A.; Hu, L.; Wang, H.; Lu, X.; Alexander, B.; Jacob, D. J. Particulate nitrate photolysis as a possible driver of rising tropospheric ozone. *Geophys. Res. Lett.* **2024**, *51* (5), No. e2023GL107980.
(88) Kong, H.; Lin, J.; Chen, L.; Zhang, Y.; Yan, Y.; Liu, M.; Ni, R.; Liu, Z.; Weng, H. Considerable Unaccounted Local Sources of NO_x Emissions in China Revealed from Satellite. *Environ. Sci. Technol.* **2022**, *56* (11), 7131−7142.
(89) Meier, S.; Koene, E. F. M.; Krol, M.; Brunner, D.; Damm, A.; Kuhlmann, G. A lightweight NO_2-to-NO_x conversion model for quantifying NO_x emissions of point sources from NO_2 satellite observations. *Atmos. Chem. Phys.* **2024**, *24* (13), 7667−7686.
(90) Clapp, L. J.; Jenkin, M. E. Analysis of the relationship between ambient levels of O_3, NO_2 and NO as a function of NO_x in the UK. *Atmos. Environ.* **2001**, *35* (36), 6391−6405.
(91) Griffin, R. J.; Beckman, P. J.; Talbot, R. W.; Sive, B. C.; Varner, R. K. Deviations from ozone photostationary state during the International Consortium for Atmospheric Research on Transport and Transformation 2004 campaign: Use of measurements and photochemical modeling to assess potential causes. *J. Geophys. Res.:Atmos.* **2007**, *112* (D10), D10S07.
(92) Lamsal, L. N.; Krotkov, N. A.; Celarier, E. A.; Swartz, W. H.; Pickering, K. E.; Bucsela, E. J.; Gleason, J. F.; Martin, R. V.; Philip, S.; Irie, H.; et al. Evaluation of OMI operational standard NO_2 column retrievals using in situ and surface-based NO_2 observations. *Atmos. Chem. Phys.* **2014**, *14* (21), 11587−11609.
(93) Li, M.; Wang, J.; Li, K.; Liu, Y.; Ochir, A.; Davaasuren, D. Assessment of grazing livestock balance on the Eastern Mongolian Plateau based on remote sensing monitoring and grassland carrying capacity evaluation. *Sci. Rep.* **2024**, *14* (1), 32151.
(94) Mukumbuta, I.; Shimizu, M.; Jin, T.; Nagatake, A.; Hata, H.; Kondo, S.; Kawai, M.; Hatano, R. Nitrous and nitric oxide emissions from a cornfield and managed grassland: 11 years of continuous measurement with manure and fertilizer applications, and land-use change. *Soil Sci. Plant Nutr.* **2017**, *63* (2), 185−199.

https://doi.org/10.1021/acs.est.6c06361
Environ. Sci. Technol. 2026, 60, 20484−20495